Green Chemistry

Accepted Manuscript

This article can be cited before page numbers have been issued, to do this please use: A. Beltram, M. Melchionna, T. Montini, L. Nasi, M. Prato and P. Fornasiero, *Green Chem.*, 2016, DOI: 10.1039/C6GC01979J.

ROYAL SOCIETY OF CHEMISTRY

www.rsc.org/greenchem

View Article Online
DOI: 10.1039/C6GC01979J

Journal Name

ARTICLE

Making H_2 from light and biomass-derived alcohols: the outstanding activity of newly designed hierarchical MWCNTs/Pd@TiO_2 hybrid catalysts

Received 00th January 20xx,
Accepted 00th January 20xx

DOI: 10.1039/x0xx00000x

www.rsc.org/

A. Beltram,[a] M. Melchionna,[a,*] T. Montini,[a, b] L. Nasi,[c] P. Fornasiero,[a, b, *] and M. Prato[a,d,e, *]

Hydrogen evolution is among the most investigated catalytic processes given the importance of H_2 from an industrial and an energy perspective. Achieving H_2 production through green routes, such as water splitting or more realistically photoreforming of alcohols, is particularly desirable. In this work, we achieve a remarkable H_2 productivity through the photoreforming of either ethanol or glycerol as sacrificial electron donor by employing a hybrid nanocatalyst where the properties of multi-wall carbon nanotubes (MWCNTs), Pd nanoparticles and crystalline TiO_2 are optimally merged through appropriate engineering of the three components and optimised synthetic protocol. Catalysts were very active both under UV (highest activity 25 mmol g^{-1} h^{-1}) and simulated solar light (1.5 mmol h^{-1} g^{-1}), as well as very stable. Critical to such high performance is the intimate contact of the three phases, each fulfilling a specific task synergistically with the other components.

Introduction

H_2 is a crucial molecule for many industrial processes including oil refining, hydrodesulfurization (HDS), hydrodenitrogenation (HDN), synthesis of NH_3 and related fertilizers and many organic hydrogenation reactions in fine chemicals production.[1] In addition, H_2 is indicated as one of the promising energy vectors of the future, even if in combination with a pool of different renewable fuels.[2] From a sustainability perspective, utilization of H_2-based energy, generated in a sustainable manner, implies a carbon-neutral footprint and therefore represents an extremely attractive option for a future switch to green methodologies. Surely, there are still many technical problems which are slowing down the implementation strategies, including the requirement for large infrastructures investments and safety issues related to H_2 storage and distribution. Another highly interesting prospect is the *in-situ* H_2 photocatalytic production to harness the green synthesis of industrially relevant molecules, a recent example being the photo-driven synthesis of benzimidazole.[3] In this complex scenario, development of efficient photocatalysts, in particular highly engineered nanocatalysts, for the generation of H_2 has become a prominent field of research.[4] Indeed, although there are several methods currently available for hydrogen production,[5] particularly desirable are those strategies based on sustainable and environmental friendly resources such as water and light.[6,7,8,9,10] Pure photocatalytic water splitting, however, still suffers from a number of shortcomings that are not of easy solution. A more realistic "clean" strategy relies on the utilization of biomass-derived species as sacrificial electron donors in the photocatalytic H_2 production process.[11,12,13,14]

Ethanol and glycerol are two biomass-derived products, the former also known as bioethanol when sustainably obtained from next-generation biomasses, such as agriculture residues or lignocellulose, and the latter representing around 10 wt % byproduct of biodiesel industry.[15] Hence, the photoreforming of ethanol and glycerol catalyzed by heterogeneous catalysts opens a very attractive route to H_2 production.[16,17,18]

As far as general heterogeneous photocatalysts are concerned, TiO_2 still represents a benchmark material due to its high activity, low cost, large availability, low toxicity and stability to corrosion.[19] However, its utilization still suffers from inherent limitations, above all the poor absorbance in the visible spectrum and therefore poor visible light photoactivity, as well as fast recombination of the photogenerated charge carriers (electrons and holes). The most popular method to improve hydrogen photo-catalytic production relies on the deposition onto the TiO_2 surface of noble metal (Au,

[a] Department of Chemical and Pharmaceutical Sciences, INSTM, University of Trieste, Via L. Giorgieri 1, 34127 Trieste, Italy.
[b] ICCOM-CNR Trieste, Via L. Giorgieri 1, 34127 Trieste, Italy.
[c] CNR-IMEM Institute, Parco area delle Scienze 37/A, 43124 Parma, Italy
[d] Nanobiotechnology Laboratory, CIC biomaGUNE, Paseo de Miramón 182, 20009 Donostia - San Sebastián, Spain
[e] Ikerbasque, Basque Foundation for Science, 48013 Bilbao, Spain

† Footnotes relating to the title and/or authors should appear here.
Electronic Supplementary Information (ESI) available: [details of any supplementary information available should be included here]. See DOI: 10.1039/x0xx00000x

View Article Online
DOI: 10.1039/C6GC01979J

Pt, Pd, Ag) and base metal (Ni, Cu) nanoparticles, that are able to capture photoexcited electrons and retard the electron/holes recombination.[20,21,22] There have been numerous reports on successful photoreforming of oxygenated compounds by TiO_2 loaded with metal nanoparticles.[11,23,24]

One recent advance in the photocatalysis by TiO_2-based catalysts is the combination of TiO_2 with carbon nanotubes (CNTs) to form nanocarbon-inorganic hybrids with improved performances.[25] CNTs have emerged as intriguing active supports in a range of catalytic applications due to their fascinating mechanical, electronic, optical and thermal properties.[26,27] In particular, as far as photocatalytic processes are concerned, reports show CNTs as active supports able to scavenge away photoexcited electrons and retard charge recombination, therefore promoting reaction rates.[28,29] Other possible mechanisms are however postulated, based for instance on a photosensitizing effect by the CNTs, which undergo the light-induced charge separation and inject the photoexcited electrons into the TiO_2 conduction band[30,31] or formation of intermediate states arising from Ti-O-C bondings such as those observed in carbon-doped TiO_2.[32,33] The effective result of the CNT-TiO_2 hybridization, when appropriately achieved, is an increased photoactivity or a significant shift of the absorbance into the visible light, both important requisites for the further developments of TiO_2-based material for H_2 photo-production. Ahmad *et al* reported on alcohol photoreforming active catalysts composed of single-walled carbon nanotubes (SWCNTs) combined with TiO_2, ascribing the improved activity to the electron sink effect generated by the SWCNT component.[34] In another report, the main factor for the successful H_2 production from triethanolamine solutions by multi-walled carbon nanotubes (MWCNTs)/TiO_2 composites loaded with Pt nanoparticles was discussed in terms of the photosensitizing by the MWCNTs.[35,36] A more recent advance in H_2 production by MWCNTs/TiO_2 composites explored the loading with other metals such as Ir, Au, Pd as well as Pt.[37] We have previously shown how a hierarchical system based on CNTs hybridized with a TiO_2 shell incorporating Pd nanoparticles shows superior photocatalytic H_2 production with respect to the conventional separated components in a model reaction test of photoreforming of methanol. The synergy between the properties of the MWCNTs and the Pd@TiO_2 structure is the key determinant for the good photocatalytic ability.[38]

Based on the above concept, in this work we have elaborated a new design for a hybrid nanomaterial incorporating functionalised MWCNTs, Pd nanoparticles and TiO_2, which fully exploits the individual component's property. As a result, we achieved high activity in photoreforming processes exploiting the use of industrially relevant biomass-derived alcohols, such as ethanol and glycerol. By careful tuning of the MWCNTs characteristics and by controlling the thermal formation of crystalline TiO_2 around the MWCNTs scaffold, we were able to prepare hybrid materials that can compete as a novel benchmark catalysts in H_2 photo-production. The catalyst is among the most active of those based on carbonaceous support. Remarkably, while the vast majority of photocatalytic systems for H_2 evolution relies on the use of the generally most active Pt active phase, we were able to surpass H_2 evolution rates by adopting the less rare and costly Pd, establishing a definite stride forward towards market feasibility. It is noteworthy that these novel catalysts can also generate H_2 from ethanol and glycerol under simulated sunlight irradiation with excellent activity, thus further expanding the significance of these catalysts for possible solar driven H_2 production.

Results and discussion

Synthetic procedures

The assembly of the nanocarbon-inorganic hybrid catalysts was carried out utilizing three building blocks: a) benzoic acid-functionalised multi-wall carbon nanotubes (*t*-MWCNTs), b) palladium nanoparticles functionalised with mercapto-undecanoic acid, c) titanium tetra-(*n*-butoxide). The synthetic scheme to access the final hybrid can be summarised in three phases (A, B and C in Figure 1). The nanotubes building block was accessed via radical addition of *in situ* formed diazonium salt of the benzoic acid (Figure 1, Step A).[39] As opposed to the oxidation treatment of CNTs, we chose this strategy for the modification of MWCNTs in order to have a more controlled functionalisation, endowing the nanotubes with COOH groups while minimising any extra damage of the polyaromatic framework by inserting additional oxygenated groups of no utility, such as epoxides or ketones. Freshly prepared Pd@TiO_2 precursors were obtained via slow addition of Pd-MUA to a THF solution of Ti(*n*-OBu)$_4$, causing the self-assembling of the Ti(*n*-OBu)$_4$ around the Pd-MUA in a core-shell configuration (Figure 1, Step B).[40] The as-functionalised MWCNTs were then reacted with the Pd-MUA@Ti(*n*-OBu)$_4$: ligand exchange between the alkoxide and the benzoic acid groups guarantee initial attachment of the inorganic nanoparticles to the *t*-MWCNTs sidewalls, with the *t*-MWCNTs then templating the growth of the oxide layer along the cylindrical scaffold. In contrast, poorer interaction between MWCNTs and Pd-MUA@Ti(*n*-OBu)$_4$ units was observed when unfunctionalised pristine nanotubes were employed, confirming that the attached benzoic acid groups serve as essential anchor points for immobilising the inorganic precursors. The relative amount of MWCNTs and Ti(*n*-OBu)$_4$ was varied in order to have two nominal compositions with 10 and 20 wt % of nanotubes, while the % of Pd remains fixed at 1.5% wt. Final hydrolysis with H_2O/THF affords the MWCNTs/Pd@TiO_2: **10-CNTs/Pd@TiO_2-fresh** (10% MWCNTs)**, 20-CNTs/Pd@TiO_2-fresh** (20% MWCNTs)) (Figure 1, step C). As part of step C, the hybrid materials were subjected to calcination at 350°C for 5 hours to give the corresponding calcined materials (**10-CNTs/Pd@TiO_2-calc**, **20-CNTs/Pd@TiO_2-calc**). For reference, the Pd@TiO_2 without MWCNTs was also prepared (**Pd@TiO_2-calc**).

View Article Online
DOI: 10.1039/C6GC01979J

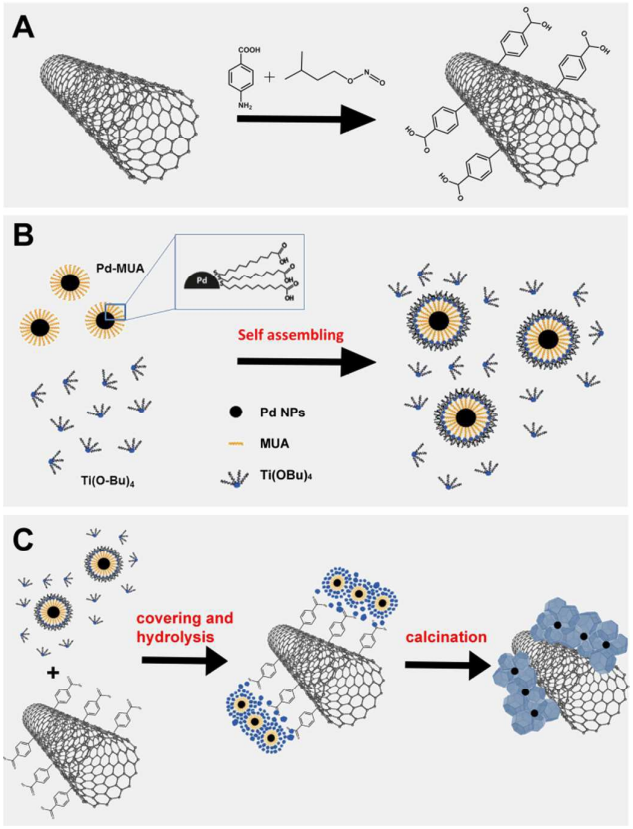

Fig 1. General Synthetic scheme of hierarchical CNTs/Pd@TiO_2-fresh and CNTs/Pd@TiO_2-calc. A) Covalent functionalisation of the MWCNTs with benzoic acid molecules through radical addition of in-situ made diazonium salt; B) Self-assembly of the Pd@TiO_2 precursor; C) hydrolysis to obtain the final hybrid, fresh and calcined.

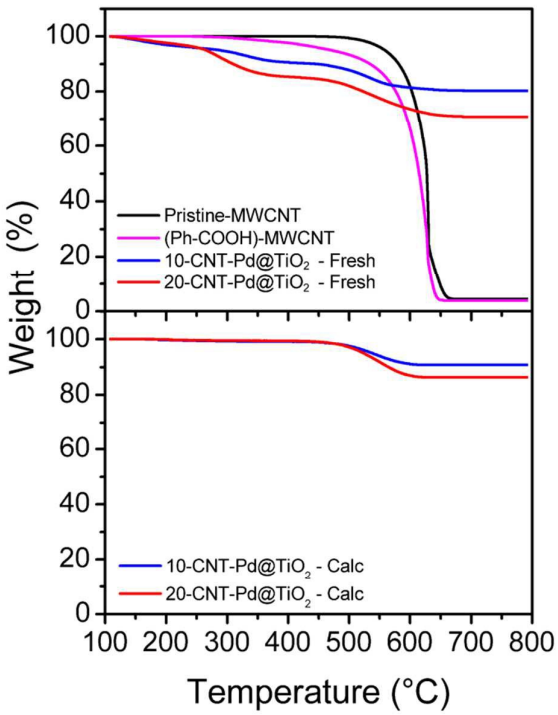

Fig 2. TGA analysis under air of the p-MWCNTs, (Ph-COOH)-MWCNTs and fresh samples after drying (top) and of the samples after calcination at 350 °C in air (bottom).

Characterisation

TGA analyses under air confirm the successful organic functionalisation of the MWCNTs and the incorporation of the three building blocks in well-defined ratios in the final hybrids. The weight loss at ~ 350 °C in the (Ph-COOH)-MWCNTs (about 3 wt%) is due to the removal of benzoic acid moieties on the nanotube sidewalls. TGA under air (Figure 2, top) exhibits the weight losses due to the oxidation of residual organic ligands (mostly butanol) around 200 °C and of the MWCNTs around 500 °C, with the remaining weight given by the inorganic components. Consistently, the calcined samples are free from the first weight losses, as the organics have been removed during calcination prior to the analysis. The content of MWCNT was estimates as ~ 9 and ~ 14 wt% for **10-CNTs/Pd@TiO_2-calc** and **20-CNTs/Pd@TiO_2-calc**, respectively (Figure 2, bottom).

Raman spectra of PhCOOH-MWCNTs shows the characteristic bands of the CNTs: the disorder-induced D band (~ 1300 cm^{-1}) with its first (~ 1600 cm^{-1}, D' band) and second-order related harmonics (~2300 cm^{-1}, 2D-band), and the G-band (~ 1590 cm^{-1}), due to the in-plane vibrational mode of the sp^2 graphitic framework. After the hybridization with Pd@TiO_2, the Raman spectra of the fresh samples (both **10-CNTs/Pd@TiO_2-fresh** and **20-CNTs/Pd@TiO_2-fresh**) suggest that TiO_2 is predominantly present as an amorphous material, as no extra peak due to crystalline TiO_2 are observed. Calcination induces the crystallization of the TiO_2 shell, as the anatase fingerprint becomes evident in the Raman spectra, with an intense band at 146 cm^{-1} and minor bands at 198 cm^{-1}, 395 cm^{-1}, 513 cm^{-1} and 639 cm^{-1}.[41, 42] In agreement, the sample **Pd@TiO_2-calc** prepared without MWCNTs showed only the bands related to the anatase phase (Figure 3, top).

In agreement with Raman analysis, XRD patterns of the samples calcined at 350°C show the typical reflections related to the anatase phase (Figure 3, bottom). Notably, no reflections can clearly be related with Pd nanoparticles, reasonably because of the low metal loading and the small average size of Pd nanoparticles, as observed by HR-TEM. The mean crystallite size of TiO_2 is not significantly affected by the formation of the hybrid materials with MWCNTs, indicating that the growth of anatase crystallites is mainly directed by the self-assembling around Pd nanoparticles.

View Article Online
DOI: 10.1039/C6GC01979J

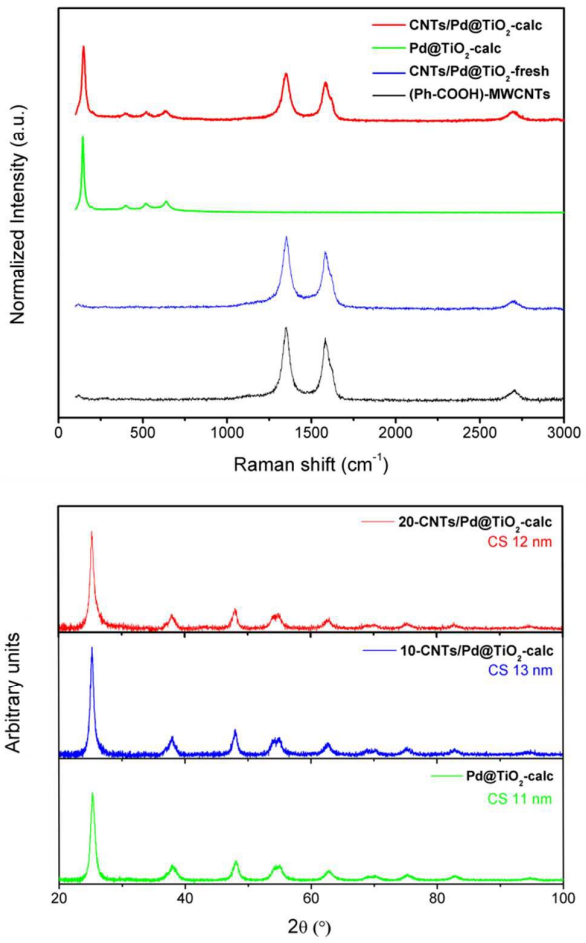

Fig 3. Comparison of the Raman spectra of the **PhCOOH-MWCNTs**, **CNT/Pd@TiO$_2$-fresh**, **CNT/Pd@TiO$_2$-calc** (top) and powder XRD patterns of **10-**, **20-CNT/Pd@TiO$_2$-calc** and **Pd@TiO$_2$-calc** (bottom). CS = mean crystallite size.

TEM micrographs confirm the successful assembly of the hybrid materials, with the calcination treatment not affecting the intimate contact between the three phases, but only the crystallinity of the TiO_2 layer. Thus, a clearly visible morphological difference between the fresh samples and the calcined samples is the diverse texture, with the latter appearing rougher, an indication of the crystallinity of the oxide layer (Figure 4). A few small regions where the nanotubes have not been covered by oxide are also observed. A combined STEM and EDX analysis provides the compositional structure, confirming the incorporation of the three components (MWCNTs, Pd and TiO_2) and their co-location (Figure 5). The non-calcined samples bear almost only amorphous TiO_2 while, as confirmed by Fast Fourier Transform (FFT) of a selected area, the calcined samples present a polycrystalline anatase phase for the TiO_2 shell, whose particle size averages 10 nm (Figure S1). The morphologies of **10-CNTs/Pd@TiO$_2$** and **20-CNTs/Pd@TiO$_2$**, both fresh and calcined samples, appear similar. As expected, an average thicker layer of TiO_2 in the former (150 nm for **10-CNTs/Pd@TiO$_2$** *vs* 120 nm for **20-CNTs/Pd@TiO$_2$**) was measured via HAADF-STM analysis, resulting from the higher loading of oxide (Figure S2). Despite being covered by the layer of TiO_2, HR-TEM analysis of **20-CNTs/Pd@TiO$_2$-calc** evidences the crystalline Pd nanoparticles, whose size ranges between 3 and 5 nm (Figure S3). The structure of the hybids after catalysis remained completely unaltered as qualitatively observed by TEM.

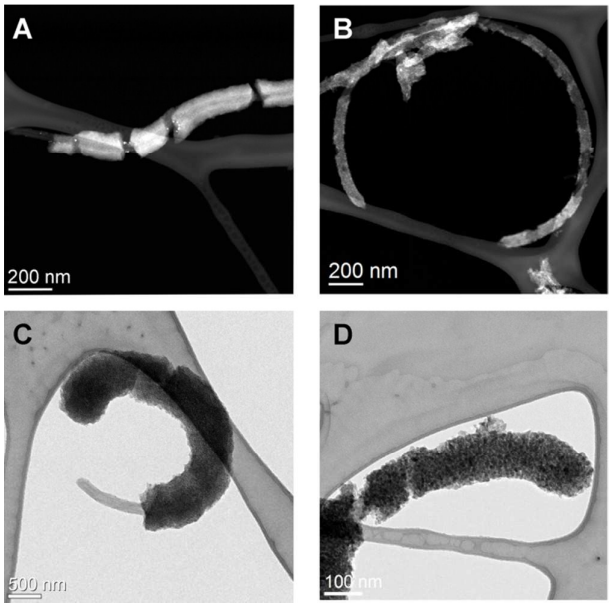

Fig 4. Representative HAADF-STEM of **20-CNTs/Pd@TiO$_2$-fresh** (A) and **20-CNTs/Pd@TiO$_2$-calc** (B). Representative TEM of **20-CNTs/Pd@TiO$_2$-fresh** (C) and **20-CNTs/Pd@TiO$_2$-calc** (D). The morphology of catalysts **10-CNTs/Pd@TiO$_2$-fresh** and **10-CNTs/Pd@TiO$_2$-calc** are similar.

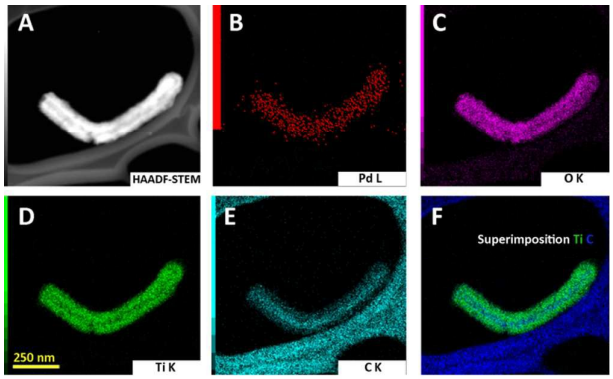

Fig. 5 A) Representative HAADF-STEM of a **CNTs/Pd@TiO$_2$-fresh**; B-E) EDX mapping showing the tight contact of the three phases: respectively palladium, oxygen, titanium, carbon; F) superimposition of EDX of the C and Ti confirming their colocation.

The textural properties of the investigated materials have been analysed by N_2 physisorption (Table 1). According to the IUPAC classification,[43] all the samples present type IV physisorption isotherms, typical of mesoporous materials (Figure 6 top). The contribution of micropores is negligible in all the investigated samples. Pristine and Ph-COOH functionalised MWCNTs present high surface areas and extended mesoporous textures, with large mesopores (10-100 nm) and high pore volumes. The textural

View Article Online
DOI: 10.1039/C6GC01979J

properties of the hybrid materials calcined at 350 °C are different: pore sizes are much smaller (in the range of 2 – 4 nm) and, as a consequence, pore volumes are reduced while specific surface areas significantly increased (Figure 6 bottom). **Pd@TiO_2-calc** material presents textural properties comparable with that the hybrid materials, confirming that the surface area and pore volume of the CNTs/Pd@TiO_2 samples are mainly related with the inorganic component.

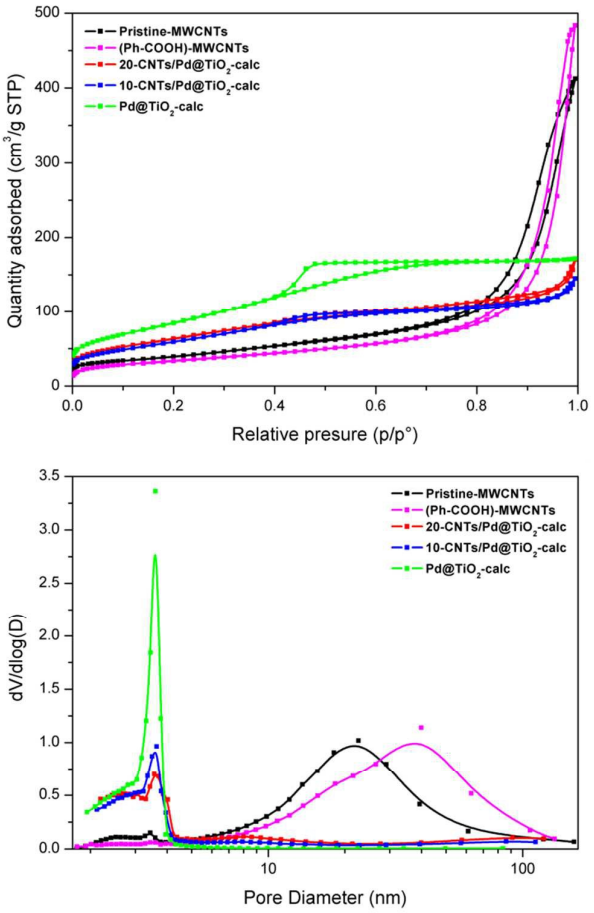

Fig 6. (top) N_2 physisorption isotherms and (bottom) BJH pore size distributions for the various materials.

Table 1. Summary of the textural properties of the investigated materials

Sample	Specific Surface Area (m^2/g)	CPV (mL/g)	D_{max} (nm)
Pristine-MWCNT	142	0.634	3.4/22
(Ph-COOH)-MWCNT	117	0.741	37
Pd@TiO_2	323	0.290	3.6
10% MWCNT	222	0.236	3.6
20% MWCNT	228	0.274	3.6

Accessibility of Pd phase has been checked by H_2 chemisorption. Samples were reduced at moderate temperature (see the Experimental section for details) to avoid significant deactivation of H_2 adsorption on Pd surface by strong metal-support interaction (SMSI) induced by the reduced TiO_2,[44, 45] and the analyses were conducted at low temperature (around -90°C using a solid/liquid acetone bath) to minimize H spillover to the reducible support.[46] Under these conditions, H_2 interaction with Pd nanoparticles results in the adsorption of H atoms on the surface and migration of H into the bulk of Pd forming Pd hydride (PdH_X).[47] The contribution of H adsorbed on the surface has been calculated by extrapolation of the linear part in the 10-20 mmHg range while the overall hydrogen consumption has been calculated after subtraction of the physisorbed H_2 by linear extrapolation of the isotherms in the range 200–400 mmHg (Figure S4). The amount of hydrogen involved in PdH_X formation has been calculated by difference of the two quantities. Table 2 summarizes the main results of H_2 chemisorption measurements. The accessibility and the dispersion of the Pd phase is significantly higher in the nanocarbon-inorganic hybrid materials with respect to the **Pd@TiO_2-calc** material. Consistently, the formation of the hybrid structure allows a more efficient encapsulation and stabilization of Pd nanoparticles, avoiding their sintering. Notably, the amount of H absorbed in the formation of PdH_X species is higher for the fully inorganic material. This result is in agreement with the dependence of solubility hydrogen in small Pd nanoparticles reported by Boudart and Hwang:[48] the larger the Pd nanoparticles, the higher the solubility of H forming PdH_X species.

Table 2. Summary of the metal textural properties of the investigated materials

Sample	H_{surf}/Pd	Metallic surface area ($m^2\ g^{-1}$)	Apparent Particle Size (nm)	X in PdH_X
Pd@TiO_2	0.20	1.4	5.5	0.77
10-CNT/Pd@TiO_2	0.50	3.4	2.2	0.45
20-CNT/Pd@TiO_2	0.52	3.5	2.1	0.33

Catalytic experiments

UV-Vis irradiation

Upon light irradiation, the PdO likely formed after the calcination treatment is reduced in situ leading to activation of the catalyst. As discussed in the introduction, the exact role of the carbon nanostructure in enhancing photocatalysis is still under debate. A plausible effect could be that of electron scavenging (Figure 7). However, given the presence of bare parts of CNTs (see TEM), the

View Article Online
DOI: 10.1039/C6GC01979J

photosensitizing could also be partially contributing, and therefore the CNTs could have multiple effects. The reaction generating H_2 implies the reduction of H^+ by the photogenerated electrons, that from the TiO_2 conduction band and are injected on Pd nanoparticles, where they are accumulated and/or consumed for reactions. (Figure 7):[49]

$$2H_{(ads)}^{+} + 2e^{-} \rightarrow H_2$$

With this consideration in mind, in order for the reduction to be efficient, another important factor is therefore the rate of diffusion of the protons, which are produced on the TiO_2 through the oxidation of the alcohol, to the Pd sites. All this implies a catalyst with very specific morphological characteristics. In this scenario, the MWCNTs would act as electron scavengers, retarding the charge recombination rates. Other possible roles for the MWCNTs, as explained in the introduction, are however plausible.

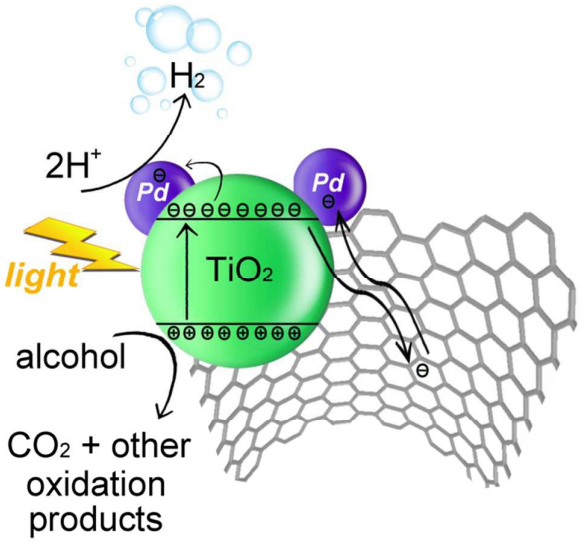

Fig 7. Scheme of a possible mechanism for H_2 generation with concomitant scavenging of the photogenerated holes by the alcohol.

The benefits of the designed synthetic protocol has been first demonstrated studying the photocatalytic H_2 production from aqueous solutions containing methanol (Figure S5). Despite not being the most sustainable choice in terms of sacrificial agent, the use of methanol allows the direct comparison of the activity of the present materials with literature data (Table S1). Together with H_2, the production of CO and CO_2 has been observed (data not shown). Fresh catalysts show a moderate activity, due to the presence of amorphous/partially crystalline TiO_2. After calcination, the H_2 production strongly increases. A similar behaviour was already reported[50] and can be related to the crystallization of the oxide shell, forming the nanocrystalline anatase with high surface area and good accessibility of the Pd active phase. Calcination also results in a tighter contact between TiO_2 and MWCNT and an increased number of heterojunctions which are key to the enhanced activity. Because of the positive effect of the thermal treatment on the performance of the present hybrid materials, only the calcined samples have been employed in the following photocatalytic studies for H_2 production using more sustainable biomass-derived sacrificial agents, i.e. ethanol and glycerol.

Under UV-vis irradiation, the amount of produced H_2 increases over time with all the investigated catalysts using both ethanol and glycerol aqueous solutions (Figure 8), as already observed for catalytic systems based on metal modified TiO_2.[51, 52, 53]

The H_2 production reaches an outstanding value of 2.4 mmol m_{cat}^{-2} for **20-CNTs/Pd@TiO_2-calc** after 24 h under UV-vis illumination, while the photocatalyst with a lower CNTs content exhibit lower activity (2.0 mmol m_{cat}^{-2}). This is a clear indication of the beneficial effect of the carbon nanotube scaffold. By comparison, the activity of the reference catalyst **Pd@TiO_2-calc** was only 0.5 mmol m_{cat}^{-2}. If reported by gram of catalysts (Figure S5), activities are among the highest ever reported for catalysts based on titania and carbonaceous supports (Table S1), with values above 25 mmol g^{-1} h^{-1} with **20-CNTs/Pd@TiO_2-calc** and 20 mmol g_{cat}^{-1} h^{-1} for **10-CNTs/Pd@TiO_2-calc**. The quantum efficiency (QE) at 365 nm of **10-CNTs/Pd@TiO_2-calc** and **20-CNTs/Pd@TiO_2-calc**, respectively 17% and 21%, confirm the promising performance of these hybrid materials.

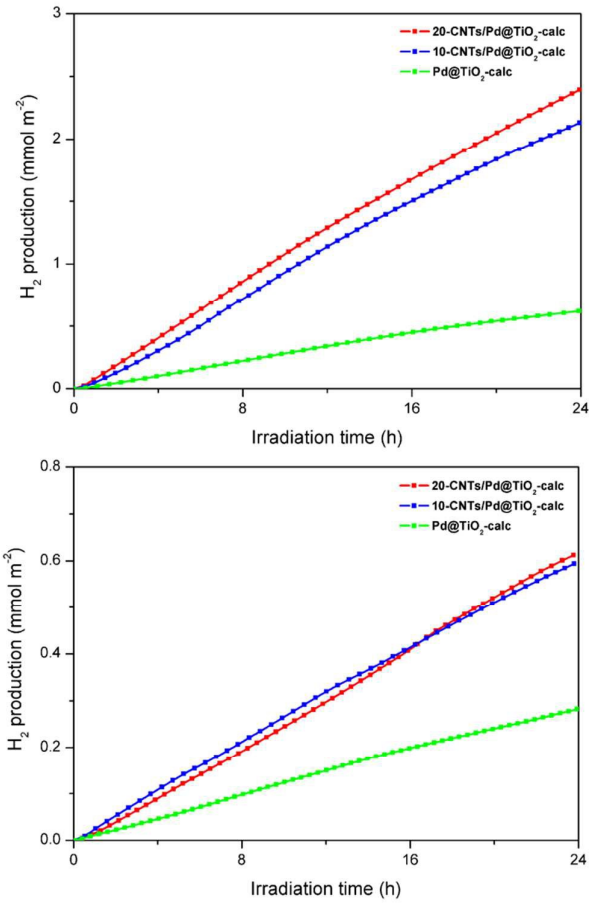

View Article Online
DOI: 10.1039/C6GC01979J

Fig 8. H_2 production over time under UV-vis illumination using aqueous solution of ethanol (top) and glycerol (bottom) as sacrificial donor. Activities are normalised by the catalyst surface areas reported in Table 1.

Investigation of the reaction by-products reveals the complexity of the network involved in the photocatalytic H_2 production. No O_2 evolution was observed, implying that the water splitting was not significantly contributing to the photocatalytic H_2 production under the present conditions. In fact, only a very small evolution of H_2 (~ 210 µmol g^{-1} h^{-1}) was measured using pure water, while the addition of methanol lead to a considerable increase in H_2 evolution rates (Figure S8).

When ethanol is used as sacrificial agent, the analysis of the gas phase evidences the presence of vapours of acetaldehyde and 1,1-diethoxyethane (its acetal with ethanol), CH_4 and CO_2 in equimolar amounts, together with ethane and traces of ethylene (Figure 9 and Figure S7). Importantly, we observed only very minor amounts of CO, this being an aspect of relevance for the application of photoreforming in fuel cells (Figure 9). Moreover, the analysis of liquid solutions recovered after photocatalytic experiments showed that the major part of acetaldehyde and 1,1-diethoxyethane were accumulated in the solutions, together with minor amount of acetic acid, 2,4,5-trimethyl-1,3-dioxolane, 3-hydroxy-2-butanone and 2,3-butandiol (Table S2).

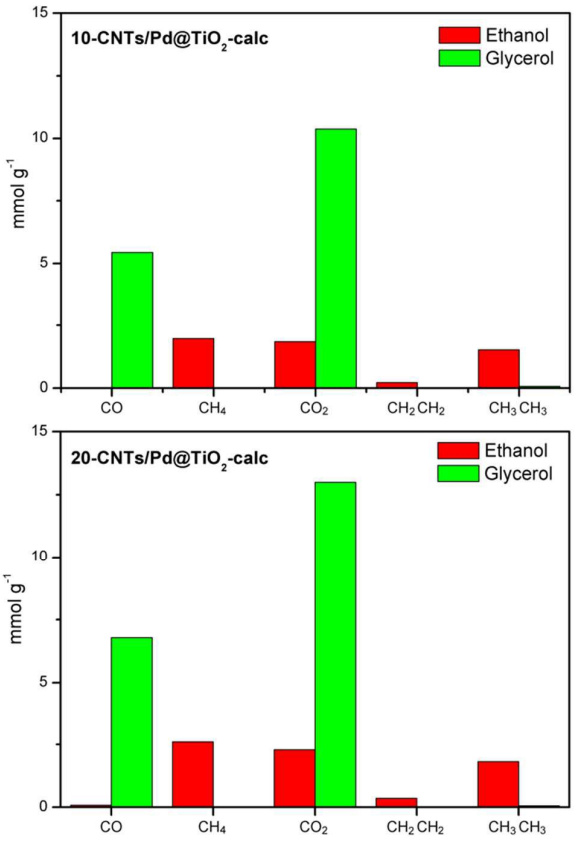

Fig 9. Amounts of by-products in the gas phase accumulated in 24 hours with **10-** and **20-CNT/Pd@TiO$_2$** for the photoreforming of ethanol and glycerol.

The detection of large quantities of by-products confirms that, in the present experimental conditions, the reforming reaction is not complete. The photodehydrogenation of ethanol to acetaldehyde is the major process involved in H_2 evolution. The stepwise oxidation of ethanol can proceed either through direct interaction with the photogenerated h^+ or indirectly by interaction with ·OH formed from the reaction $H_2O_{ads} + h^+ \rightarrow \cdot OH_{ads} + H^+_{ads}$.[54, 55] Most likely, the two oxidation pathways are simultaneously proceeding. Oxidation of acetaldehyde to acetic acid is considered to be the rate determining step with TiO_2 catalysts in alcohol photoreforming.[58] Given the low adsorption capability of the acetaldehyde onto the TiO_2, it can easily reacts with ethanol forming the acetal 1,1-diethoxyethane while the formation of traces of acetic acid is expected to occur through oxidation in solution by some radical species formed *in situ* (mainly ·OH). The formation of CH_4 and CO_2 in equimolar amounts indicates that these gases are formed by direct decomposition of acetic acid or by decomposition of acetaldehyde to CH_4 and CO, followed by oxidation of CO to CO_2 through a "photocatalytic Water Gas Shift Reaction". Together with methane and CO_2, the presence of ethane could also arise through a radical mechanism, namely from the radical coupling of $\cdot CH_3$, or by hydrogenation of ethylene formed from ethanol on the acid sites of the oxide. The contribution of acetaldehyde photodecomposition was confirmed by performing a photocatalytic experiment using acetaldehyde as sacrificial agent, added after 3 h of irradiation of the photocatalysts in pure water (Figure S9). After acetaldehyde addition, H_2 is produced in major amount, together with CH_4, CO_2 and traces of ethane.

Among the other by-products accumulated in solution during ethanol photoreforming, 2,3-butandiol is probably formed through radical C-C coupling of two ethanol molecules. From this compound, 3-hydroxy-2-butanone is formed by dehydrogenation from one OH group while 2,4,5-trimethyl-1,3-dioxolane is formed by reaction of 2,3-butandiol with acetaldehyde.

In the case of glycerol, lower H_2 production rates were observed for all the investigated catalysts (Figure 8 and Figure S6). Both **10-** and **20-CNT/Pd@TiO$_2$** displayed an activity normalised by the surface area of 0.6 mmol m_{cat}^{-2}, while that of **Pd@TiO$_2$-calc** was only 0.3 mmol m_{cat}^{-2}. Analysis of by-products in the gas phase revealed that both CO_2 and CO are present together with trace amounts of ethane, with their formation rate increasing over time (Figure 9 and Figure S10). Semi-quantitative GC/MS analysis of the solutions recovered after photocatalytic experiments evidenced the accumulation of non-volatile by-products. Hydroxyl acetaldehyde, 1-hydroxy-2-propanone and 1,3-dihydroxy-2-propanone were the most abundant, followed by formic acid and 2,3-dihydroxy-propanal and trace amounts of acetic acid.

Differently from the case of ethanol, the carbonylic compounds formed by the first dehydrogenation of glycerol – 2,3-dihydroxy-propanal and 1,3-dihydroxy-2-propanone – still contain OH groups, that allow their adsorption on the TiO_2 surface and the competition with glycerol to be oxidised by the holes. The results clearly indicate

View Article Online
DOI: 10.1039/C6GC01979J

that oxidation/degradation of 2,3-dihydroxy-propanal is much easier than that of 1,3-dihydroxy-2-propanone. CO and CO_2 formation are usually related to the photocatalytic degradation of carbonylic and carboxylic intermediate compounds, formed by progressive dehydrogenation of the glycerol molecule, mainly through 2,3-dihydroxy-propanal and leading to intermediate smaller compounds (hydroxyl acetaldehyde, formic acid and acetic acid).[52] On the other hand, 1-hydroxy-2-propanone is presumably formed on the surface of the titania via dehydration/hydrogenation from 1,3-dihydroxy-2-propanone, hardly oxidised/decomposed on TiO_2 surface by holes, or directly by dehydration of glycerol. The formation of added value organic by-products in both ethanol and glycerol photoreforming can lead to extra valorization of biomasses.[18] However, this is only viable if the products can be easily separated or if the oxidation of the alcohol proceeds selectively. This aspect opens the doors to studies on contact times between the reactant and the catalyst, sparking exploration of the correct engineering of flow reactors.

Simulated solar irradiation

When irradiated with a simulated solar light, both **10-CNTs/Pd@TiO_2-calc** and **20-CNTs/Pd@TiO_2-calc** display an appreciable activity for the photoreforming of ethanol, although lower than the corresponding UV-irradiated samples. The drop in activity is somehow expected as the TiO_2 can only absorb the small UV percentage of incident radiation. However, the detected activity provide a platform for these hybrid systems to be used with solar light (Figure 10, top).

When EtOH is employed as sacrificial electron donor, the catalyst **20-CNTs/Pd@TiO_2-calc** shows a H_2 productivity of 120 µmol m_{cat}^{-2} in 24 h, while for the **10-CNTs/Pd@TiO_2-calc** the productivity was slightly higher (140 µmol m_{cat}^{-2}). Interestingly, as compared to the UV experiments, the activity of the two catalysts with different CNT contents is inversed under simulated solar irradiation. Both catalysts are still more active than the reference catalyst **Pd@TiO_2-calc** (87 µmol m_{cat}^{-2}). It is also worth noting that the two CNT-based catalysts undergo a progressive activation over the initial 4 hours before reaching a constant H_2 evolution rate, while the CNT-free material shows stable activity from the beginning of the experiment. Remarkably, and in contrast to the UV experiments, the activity of all the catalysts with glycerol used as sacrificial donor, does not decrease significantly (Figure 10, bottom). On the contrary, for **10-CNTs/Pd@TiO_2-calc** and **Pd@TiO_2-calc** the H_2 productivity is even slightly higher (149 µmol m_{cat}^{-2} and 107 µmol m_{cat}^{-2}), while for **20-CNTs/Pd@TiO_2-calc** slightly diminishes to 95 µmol m_{cat}^{-2}. This suggests that the rate-determining step does not depend on the sacrificial electron donor or on the diffusion of the adsorbed protons from TiO_2 to the Pd sites. Rather, it must be associated with the rate of formation of the charge carriers generated upon irradiation, which is considerably lower than that under UV. It is therefore acceptable to assume that once the fraction of electrons and holes are formed, they are immediately quenched by the (respectively) electron acceptor (protons) and electron donors (alcohol). As expected, when ethanol is used as sacrificial donor, analysis of the liquid phase shows two main products, acetaldehyde and 1,1-diethoxyethane in amounts proportional to the produced H_2 if compared to the UV experiments (Table S4). With glycerol, we found as main liquid by-product one of the expected first oxidation products, namely 1,3-dihydroxy 2-propanone, 1-hydroxy-2-propanone and hydroxyl-acetaldehyde, in analogy with the UV experiment (Table S5).

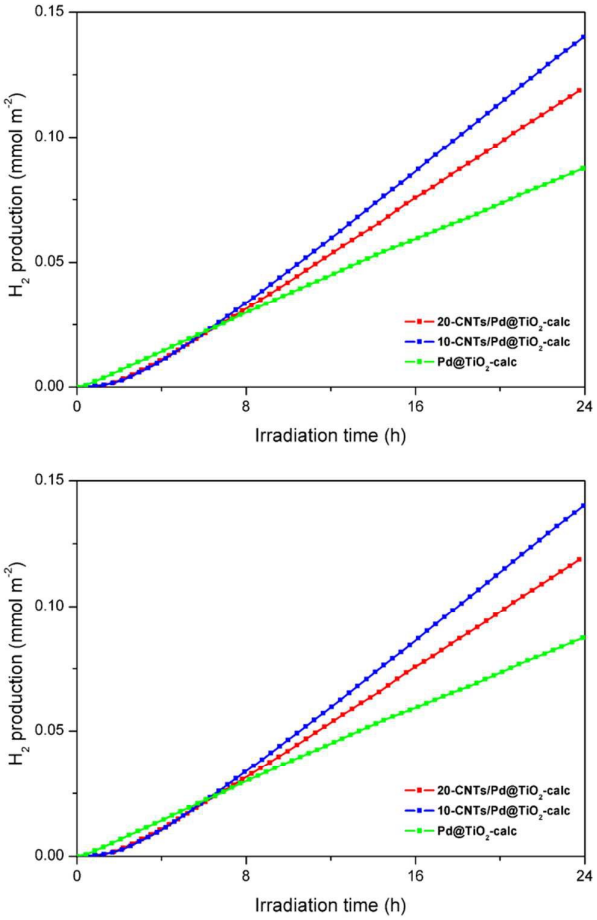

Fig 10. H_2 production over time under simulated solar illumination using ethanol (top) and glycerol (bottom) as sacrificial donor. Activities are reported normalised by the catalyst surface area as calculated in table 1.

Experimental

Functionalisation of the multi-wall carbon nanotubes (PhCOOH-MWCNTs)

100 mg of pristine MWCNT purchased from Nanoamor (20–30 nm diameter and 0.5–2 µm length) were dispersed in 100 mL of H_2O by sonication for 20 minutes. Then the p-amino-benzoic acid (3.3 equivalents respect to carbon moles in the MWCNTs) was added and mixed by sonication for further 10 minutes. The mixture was put under vigorous stirring and 2.25 mL of isopentyl nitrite were added just before start the heating treatment at 80 °C for 6 h under

View Article Online
DOI: 10.1039/C6GC01979J

reflux. **Caution**: diazonium salts should be handled with care since they can be explosive. The mixture was naturally cooled down at room temperature and collected by filtration on a 0.1 µm polytetrafluoroethylene Millipore membrane. Finally the material was washed with DMF, MeOH, H_2O, EtOH and Et_2O sonicating the solid for 5 minutes in each solvent and dried overnight at 80 °C.

Synthesis of MWCNT-Pd@TiO_2 hybrids

The composite materials were prepared employing 0, 10 and 20 mg of *f*-MWCNT and respectively labelled **10-CNTs/Pd@TiO_2, 20-CNTs/Pd@TiO_2 and Pd@TiO_2.** The *f*-MWCNT were dispersed in absolute ethanol (EtOH mL/*f*-MWCNT mg ratio: 2.5) by sonication for 30 minutes meanwhile a Pd-MUA THF solution (containing 1.5 mg of Pd) was slowly added to a THF solution of Ti(O-*n*-Bu)$_4$ (containing 98.5, 88.5 and 78.5 mg of TiO_2 respectively). Then the Pd@TiO_2 precursors solution was slowly added under sonication to the *f*-MWCNT dispersion and the mixture was further sonicated for 30 minutes. Finally a 10% solution of H_2O in EtOH (Ti(*n*-OBu)$_4$ /H_2O molar ratio: 1/120) was dropped and the mixture sonicated for 30 minutes. The materials were collected by filtration on a 0.45 µm polytetrafluoroethylene Millipore membrane, washed with ethanol and dried overnight at 80 °C. In order to eliminate the organic ligands and improve the crystallization of the TiO_2 (see discussion below) the catalyst were subjected to calcination at 350 °C for 5 hrs (+3 °C/min; -4.5 °C/min).

Characterisation

X-ray Diffraction (XRD) patterns were collected on a Philips X'Pert diffractometer using a monochromatized Cu Kα (λ = 0.154 nm) X-ray source in the range 20° < 2θ < 100°. The mean crystallite sizes of the TiO_2 were calculated by applying the Scherrer equation to the (101) reflection of anatase phase.

Thermogravimetric analysis (TGA) was performed on TGA Q500 (TA Instruments) under air or nitrogen, equilibrating the temperature at 100°C and heating at 10 °C min^{-1} up to 800 °C.

Raman spectra were recorded on a inVia Renishaw microspectrometer equipped with a Nd:YAG laser using an excitation wavelength of 532 nm. The dispersed samples were drop casted onto silicon wafers and analysed in 5 different point subsequently averaged.

TEM measurements were performed on a TEM Philips EM208, using an acceleration voltage of 100kV. Samples were prepared by drop casting the dispersed particles onto a TEM grid (200 mesh, copper, carbon only). High resolution TEM (HRTEM) were acquired on a JEOL 2200FS microscope operating at 200 kV, equipped with an Energy Dispersive Spectrometer (EDS), in-column energy (Omega) filter, and High-Angle Annular Dark-Field (HAADF) detector.

N_2 physisorption isotherms were recorded at liquid nitrogen temperature using a Micrometrics ASAP 2020 automatic analyser. The samples were degassed in vacuum at 120 °C for 12 h before analysis.

H_2 chemisorption was performed using a Micrometrics ASAP 2020C apparatus. A chemisorption stoichiometry H:M = 1:1 was assumed for the calculation of the exposed metal surface area. The materials has been pre-reduced in a flow of H_2 (5%)/Ar (40mL/min) at 100°C for 30 minutes and degassed at 250°C for 5 hours. H_2 chemisorption isotherms has been recorded in 1 – 400 torr pressure range at around -90°C (solid/liquid acetone bath).

Catalytic tests and quantum efficiency measurement

It is known that the mechanism and therefore the H_2 evolution depend on the sacrificial agent concentration. [56, 57] In the present experiments, ethanol and glycerol concentrations have been chosen in order to better represent aqueous solutions deriving from plants of the treatment of biomasses. Ethanol/water 50:50 solutions are representative of a solution coming from fermentation plants without being subjected to deep purification by distillation (a highly energy consuming industrial step). Glycerol 1M solution has a composition close to that deriving from biodiesel production plants. Moreover, the duration of each experiment has been optimized to minimize evaporation of the solution, in order to avoid significant variations of the alcohol/water ratios.

The materials were tested as photocatalyst for hydrogen production by photoreforming of ethanol (50% v/v) and glycerol (1 M) under two different light source apparatus: a Teflon-lined photoreactor illuminate with a Lot-Oriel Solar Simulator equipped with a 150 W Xe lamp and an Atmospheric Edge Filter with a cut-off at 300 nm and a Pyrex photoreactor illuminated with a 125 W medium pressure Hg lamp (model UV13F, Helios Italquartz, Italy). In a typically catalytic test 10 mg of the calcined material was prior suspended in the photoreactor by sonication for 10 minutes in 60 mL of alcohol solution and subsequently purged from air with Ar flow of 15 mL min^{-1} for 40 minutes and thermostated at 20 °C. During the purge and the catalytic test the materials were magnetically stirred.

The on-line detection of volatile products was carried out using a Gas Chromatograph equipped with two analytical lines and a 10 way-two loops injection valve was employed for injection during on-line analysis of the gaseous products. In the former apparatus an Agilent 7890A Gas Chromatograph equipped with a Carboxen 1010 PLOT (Supelco, 30 m x 0.53 mm ID, 30 µm film) column followed by a Thermal Conductivity Detector (TCD) was used for gaseous products quantification using Ar as carrier and a DB-225ms column (J&W, 60 m x 0.32 mm ID, 20 µm film) using He as carrier followed by a mass spectrometer (MS) HP 5975C was employed for the detection of the volatile organic compounds. In the later apparatus an Agilent 6890N Gas Chromatograph equipped with a MolSieve 5Å (Restek, 30 m x 0.53 mm ID) column followed by a Thermal Conductivity Detector (TCD) was used for gaseous products quantification using Ar as carrier and a PoraPlot Q (Agilent, 30 m x

View Article Online
DOI: 10.1039/C6GC01979J

0.53 mm ID, 40 µm film) column using Ar as a carrier followed by a methanator and a Flame Ionization Detector (FID) was employed for the detection of the volatile organic compounds.

After the photocatalytic tests, the liquid phases were separated from the catalyst by filtration on a 0.45 µm PVDF Millipore membrane and subsequently analysed by GC/MS to detect the by-products accumulated. For a semi-quantitative analysis, 1-butanol and 1-esanol were used as internal standard in the liquid phases recovered from ethanol and glycerol tests, respectively.

Quantum efficiency (QE) was calculated with equation:

$$QE = 2 \cdot \text{mol } H_2 \text{ / absorbed photons}$$

irradiating the sample with a 4 W Hg Penray.

Conclusions

Development of new nanostructured catalysts for the sustainable production of H_2 has become one of the most fertile fields of research in catalysis, given the central position of the H_2 molecule in industry and energy-related applications. Our approach is based on the recognition that functional multicomponent materials are leveraged to the H_2 production with unmatched efficiency, provided that each component is appropriately endowed with the required characteristics for the specific role. Here, we have engineered and accurately interlaced three nanoscale elements, namely i) functionalised MWCNTs, ii) functionalised (3-5 nm) Pd nanoparticles and iii) crystalline TiO_2 in a precise hierarchical order. The hybrid catalyst is able to drive the light-induced (both UV and solar simulated irradiation) H_2 evolution from biomass-derived alcohols (ethanol and glycerol) with production rates which are amongst the best reported for carbon-supported catalysts, with highest activity (under UV) setting at 2.4 mmol m_{cat}^{-2} after 24 hours (rate per gram: 25 mmol g^{-1} h^{-1}). By comparing with the state-of-the-art photocatalysts, the definite step forward arises from several advantages, such : 1) the use of lower-powered irradiation lamps, 2) the use of Pd in lieu of the intrinsically more active, but more costly, Pt, 3) the replacement of generally used methanol as sacrificial electron donor with alcohols of higher value. All these advantages are realized without compromising the H_2 productivity. The outstanding performance of the catalysts critically depends on the developed synthetic protocols, allowing a uniform and tight interfacing of the three components, which can therefore work in perfect synergy. The catalysts also exhibit excellent stability over at least 24 h. Last, in the wider view, the anatomy of the synthetic photocatalyst to unveil the corresponding structure/reactivity relationships is expected to provide the key guidelines to evolve a new generation of carbon supported catalysts for artificial water splitting.

Acknowledgements

The research leading to these results has received funding from the University of Trieste (project FRA2015), INSTM, the Seventh Framework Programme [FP7/2007- 2013] under grant agreement n° 310651 (SACS project). Dr. A. Aneggi and prof. A. Trovarelli (University of Udine, Italy) are kindly acknowledged for access to XRD facility.

Notes and references

‡ Footnotes relating to the main text should appear here. These might include comments relevant to but not central to the matter under discussion, limited experimental and spectral data, and crystallographic data.
§
§§
etc.

1 N. Armaroli and V. Balzani, *ChemSusChem*, 2011, **4**, 21.
2 S. Zinoviev, F. Müller-Langer, P. Das, N. Bertero, P. Fornasiero, M. Kaltschmitt , G. Centi and S. Miertus, *ChemSusChem*, 2010, **3**, 1106.
3 Y. Shiraishi, Y. Sugano, S. Tanaka and T. Hirai, *Angew. Chem. Int. Ed.,* 2010, **49**, 1656.
4 M. Cargnello, T. Montini, S. Y. Smolin, J. B. Priebe, J. J. Delgado Jaèn, V. V. T. Doan-Nguyen, I. S. McKay, J. A. Schwalbe, M. M. Pohl, T. R. Gordon, Y. Lu, J. B. Baxter, A. Brückner, P. Fornasiero and C. B. Murray, *Proc. Natl. Acad. Sci. U.S.A.*, 2016, **113**, 3966.
5 K. Liu, C. Song and V. Subramani, Hydrogen and Syngas Production and Purification Technologies, Wiley, Hoboken, 2010.
6 A. Fujishima and K. Honda, *Nature*, 1972, **238**, 37.
7 V. Balzani, A. Credi and M. Venturi, *ChemSusChem*, 2008, **1**, 26.
8 H. B. Gray, *Nature Chem.,* **1**, 7.
9 N. S. Lewis and D. G. Nocera, *Proc. Natl Acad. Sci. USA*, 2006, **103**, 15729.
10 K. Jun, Y. S. Lee, T. Buonassisi and J. M. Jacobson, *Angew. Chem. Int. Ed.*, 2012, **51**, 423.
11 A. Gallo, T. Montini, M. Marelli, A. Minguzzi, V. Gombac, R. Psaro, P. Fornasiero and V. Dal Santo, *ChemSusChem*, 2012, **5**, 1800.
12 D. Barreca, G. Carraro, V. Gombac, A. Gasparotto, C. Maccato, P. Fornasiero and E. Tondello, *Adv. Funct. Mater.*, 2011, **21**, 2611.
13 K. Shimura and H. Yoshida, *Energy Environ. Sci.*, 2011, **4**, 2467.
14 X. Chen, S. Shen, L. Guo and S. S. Mao, *Chem. Rev.,* 2010, **110**, 6503.
15 S. Zinoviev, F. Müller-Langer, P. Das, N. Bertero, P. Fornasiero, M. Kaltschmitt, G. Centi and S. Miertus, *ChemSusChem*, 2010, **3**, 1106.
16 T. Montini, M. Monai, A. Beltram, I. Romero-Ocaña and P. Fornasiero, *Mater. Sci. Semicond. Process*., 2016, **42**, 122.
17 A. V. Puga, *Coord. Chem. Rev.,* 2016, **315**, 1.
18 M. Cargnello, A. Gasparotto, V. Gombac, T. Montini, D. Barreca and Paolo Fornasiero, *Eur. J. Inorg. Chem*., 2011, **28**, 4309.
19 O. Carp, C. L. Huisman and A. Reller, *Prog. Solid State Chem*., 2004, **32**, 33.
20 A. Primo, A. Corma and H. Garcia, *Phys. Chem. Chem. Phys.*, 2011, **13**, 886.
21 T. Montini, V. Gombac, L. Sordelli, J. J. Delgado, X. Chen, G. Adami and P. Fornasiero, *ChemCatChem*, 2011, **3**, 574.
22 A. V. Korzhak, N. I. Ermokhina, A. L. Stroyuk, V. K. Bukhtiyarov, A. E. Raevskaya, V. I. Litvin, S. Ya. Kuchmiy, V. G.

View Article Online
DOI: 10.1039/C6GC01979J

Ilyin and P. A. Manorik, *J. Photochem. Photobiol. A*, 2008, **198**, 126.
23 M. Bowker, C. Morton, J. Kennedy, H. Bahru, J. Greves, W. Jones, P.R. Davies, C. Brookes, P.P. Wells and N. Dimitratos, *J. Catal.*, 2014, **310**, 10.
24 X. Chen, L. Liu, P. Y. Yu and S. S. Mao, *Science*, 2011, **331**, 746.
25 D. Eder, *Chem. Rev.*, 2010, **110**, 1348.
26 M. Melchionna, M. Bonchio, F. Paolucci, M. Prato and P. Fornasiero, *Top Curr. Chem.,* 2014, **348**, 139.
27 M. Melchionna, S. Marchesan, M. Prato and P. Fornasiero, *Catal. Sci. Technol*., 2015, **5**, 3859.
28 K. Woan, G. Pyrgiotakis and W. Sigmund, *Adv. Mater.*, 2009, **21**, 2233.
29 Y. Yu, J. C. Yu, J. G. Yu, Y. C. Kwok, Y. K. Che, J. C. Zhao, L. Ding, W. K. Ge and P. K. Wong, *Appl. Catal. A*, 2005, **289**, 186.
30 W. Wang, P. Serp, P. Kalck and J. L. Faria, *J. Mol. Catal. A-Chem.*, 2005, **235**, 194.
31 W.-D. Zhang, B. Xu and L.-C. Jiang, *J. Mater. Chem*., 2010, **20**, 6383.
32 S. Sakthivel and H. Kisch, *Angew. Chem. Int. Ed*., 2003, **42**, 4908.
33 L.-C. Chen, Y.-C. Ho, W.-S. Guo, C.-M. Huang and T.-C. Pan, *Electrochim. Acta*, 2009, **54**, 3884.
34 B. Ahmmad, Y. Kusumoto, S. Somekawa and M. Ikeda, *Catal. Commun*., 2008, **9**, 1410.
35 K. Dai, T. Peng, D. Ke and B. Wei, *Nanotechnology*, 2009, **20**, 124603.
36 K. Dai, X. Zhang, K. Fan, P. Zeng and T. Peng, *J. Nanomater*., 2014, **2014**, 694073.
37 C. G. Silva, M. J. Sampaio, R. R.N. Marques, L. A. Ferreira, P. B. Tavares, A. M.T. Silva and J. L. Faria, *Appl Catal B: Enivronmental*, 2015, **178**, 82.
38 M. Cargnello, M. Grzelczak, B. Rodrıguez-Gonzalez, Z. Syrgiannis, K. Bakhmutsky, V. La Parola, L. M. Liz-Marzan, R. J. Gorte, M. Prato and P. Fornasiero, *J. Am. Chem. Soc.*, 2012 **134**, 11760.
39 J. L. Bahr and J. M. Tour, *Chem. Mater.,* 2001**, 13**, 3823.
40 K. Bakhmutsky, N. L. Wieder, M. Cargnello, B. Galloway, P. Fornasiero and R. J. Gorte, *ChemSusChem*, 2012, **5**, 140.
41 T. Ohsaka, F. Izumi, and Y. Fujiki, *J. Raman Spectrosc*. 1978, **7**, 321.
42 O. Frank, M. Zukalova, B. Laskova, J. Kürti, J. Koltai and L. Kavan, *Phys. Chem. Chem. Phys*., 2012, **14**, 14567.
43 K. S. W. Sing, D. H. Everett, R. A. W. Haul, L. Moscou, R. A. Pierotti, J. Rouquerol and T. Siemieniewska, *Pure Appl. Chem.*, 185, **57**, 603.
44 J. H. Kang, E. W. Shin, W. J. Kim, J. D. Park and S. H. Moon, *J. Catal.*, 2002, **208**, 310.
45 Y. Li, B. Xu, Y. Fan, N. Feng, A. Qiu, J. M. J. He, H. Yang and Y. Chen, *J. Mol. Catal. A: Chem.*, 2004, **216**, 107.
46 J. M. Gatica, R. T. Baker, P. Fornasiero, S. Bernal, G. Blanco and J. Kašpar, *J. Phys. Chem. B*, 2000, **104**, 4667.
47 J. M. Gatica, R. T. Baker, P. Fornasiero, S. Bernal and Jan Kašpar, *J. Phys. Chem. B*, 2001, **105**, 1191.
48 M. Boudart and H. S. Hwang, *J. Catal*., 1975, **39**, 44.
49 D. W. Bahnemann, M. Hilgendorff, R. Memming, *J. Phys. Chem. B*, 1997, **101**, 4265.
50 M. Melchionna, A. Beltram, T. Montini, M. Monai, L. Nasi, P. Fornasiero and M. Prato, *Chem. Commun.*, 2016, **52**, 764.
51 G. L. Chiarello, M. H. Aguirre, E. Selli, *J. Catal*., 2010, **273**, 182.
52 T. Montini, V. Gombac, L. Sordelli, J. J. Delgado, X. Chen, G. Adami and P. Fornasiero, *ChemCatChem*, 2010, **3**, 574.
53 C. Ampelli, R. Passalacqua, C. Genovese, S. Perathoner, G. Centi, T. Montini, V. Gombac, J. J. Delgado Jaen and P. Fornasiero, *RSC Adv*., 2013, **3**, 21776.
54 J. M. Kesselman, O. Weres, N. S. Lewis and M. R. Hoffmann, *J. Phys. Chem. B*, 1997, **101**, 2637.
55 C. Y. Wang, R. Pagel, D. W. Bahnemann, J. K. Dohrmann, *J. Phys. Chem. B*, 2004, **108**, 14082.
56 G. L. Chiarello, D. Ferri and E. Selli, *J. Catal.*, 2011, **280**, 168.
57 D. I. Kondarides, A. Patsoura and X. E. Verykios, *J. Adv. Oxid. Technol.*, 2010, **13**, 116.